Journal of Alloys and Compounds 1060 (2026) 187245

Contents lists available at ScienceDirect

Journal of Alloys and Compounds

journal homepage: www.elsevier.com/locate/jalcom

Unveiling atomic-scale transport for giant tunnel magnetoresistance in $Co_{47}Mn_{32}Si_{21}$/MgO/$Co_{47}Mn_{32}Si_{21}$ magnetic tunnel junctions

M. Zenati [a,b], D. Bensaid [a,b], M.R. Chellali [c,*]

[a] Exact Science Faculty, Djillali Liabes University of Sidi Bel Abbes, Algeria
[b] Magnetic Materials Laboratory, Djillali Liabès University, BP89, Sidi-Bel-Abbès 22000, Algeria
[c] Institute of Nanotechnology, Karlsruhe Institute of Technology, Eggenstein-Leopoldshafen 76344, Germany

ARTICLE INFO

Keywords:
CoMnSi
MgO
Tunnel magnetoresistance
Activation energy
Interface engineering

ABSTRACT

Mn diffusion in $Co_{47}Mn_{32}Si_{21}$/MgO/$Co_{47}Mn_{32}Si_{21}$ magnetic tunnel junctions (MTJs) plays a crucial role in interface stability, spin polarization, and tunnel magnetoresistance (TMR). Up to 823 K, Mn remains confined to grain boundaries, preserving structural order and facilitating coherent tunneling. The extracted activation energy of 73.11 kJ/mol confirms grain boundary diffusion as the dominant atomic transport mechanism. Beyond this, Mn migration into MgO barrier contributes to structural degradation and a reduction in tunnel magnetoresistance (TMR) performance. Maximum TMR ratios of 1995% at 4.2 K and 378% at room temperature, exceeding those of MTJs with nearly stoichiometric CoMnSi electrodes, highlight the critical importance of interface engineering. The observed TMR enhancement correlates primarily with annealing-driven improvements in crystallinity and interface quality, while Mn redistribution provides additional mechanistic insight into thermally activated interfacial diffusion processes.

1. Introduction

Spintronics, which exploits the electron spin degree of freedom in addition to charge, has emerged as a promising platform for high-speed, energy-efficient, and nonvolatile microelectronic devices, including magnetic memories, sensing technologies, and emerging computing architectures [1–3]. Magnetic tunnel junctions (MTJs) with MgO barriers have demonstrated exceptional tunnel magnetoresistance (TMR) due to coherent Δ_1 electron transport [4], significantly outperforming conventional AlO_x-based MTJs [5,6]. Among spintronic materials, Co-based Heusler alloys are ideal candidates due to their high Curie temperatures (400–1200 K) and predicted half-metallicity [7], making them highly attractive for MTJs [8]. Early studies reported a 16% TMR ratio at room temperature in $Co_2Cr_{0.6}Fe_{0.4}Al$/AlO_x/CoFe MTJs [9], while later advances in Co_2MnSi/MgO MTJs achieved 753% at 2 K and 217% at room temperature [10]. Fully epitaxial Co_2MnSi/MgO/Co_2MnSi MTJs have since demonstrated TMR ratios of 236% at room temperature and 1135% at 4.2 K [11,12], reinforcing their potential for spintronic applications. Additionally, Co_2MnSi-based MTJs have demonstrated a tunnel magnetoresistance ratio of ~203% at 2 K, further supporting their suitability for spin-dependent transport [13]. Integrating a Heusler alloy upper electrode with an MgO barrier mitigates conductivity mismatch, improving spin injection and device performance [14]. Despite these advantages, interfacial disorder and elemental migration in Co-based Heusler MTJs can degrade TMR by disrupting Δ_1 electron transport [11,15]. High-temperature annealing, while crucial for optimizing magnetic properties, can exacerbate these issues, particularly through manganese (Mn) diffusion, which reduces TMR and can even reverse exchange bias in synthetic antiferromagnets [16]. Thermal stability remains a key challenge, as studies show that while moderate annealing (~483 K) enhances TMR [17], prolonged exposure to higher temperatures leads to performance degradation. In Co/Al_2O_3/Co junctions, TMR increases up to 480 K but declines at 530 K, breaking down beyond 600 K [18]. These findings highlight the need for precise thermal management to balance performance optimization and interfacial stability.

The current study aims to (i) investigate the structural, chemical, and magnetic properties of $Co_{47}Mn_{32}Si_{21}$ films used as both lower and upper electrodes, along with an MgO barrier, as a function of annealing temperature (T_a), and (ii) achieve the highest possible TMR through optimized fabrication conditions. To understand the effects of annealing on atomic-scale composition and diffusion behavior, Atom Probe Tomography (APT) was employed to analyze chemical distribution across interfaces and tunnel barriers in $Co_{47}Mn_{32}Si_{21}$/MgO-based magnetic

* Corresponding author.
E-mail address: m_chel01@uni-muenster.de (M.R. Chellali).

https://doi.org/10.1016/j.jallcom.2026.187245
Received 23 December 2025; Received in revised form 28 February 2026; Accepted 6 March 2026
Available online 7 March 2026

tunnel junctions. APT provides key insights into atomic rearrangements and interfacial stability [19], linking microstructure to spin-dependent transport. While TEM has been widely used for interface studies, its atomic-scale resolution is limited by imaging misalignment [5,20]. In contrast, APT enables three-dimensional atomic-resolution imaging, offering a more precise assessment of elemental redistribution, essential for optimizing MTJ performance and long-term stability.

2. Experimental details

All samples were fabricated using radio-frequency (RF) and direct current (DC) magnetron sputtering under ultrahigh vacuum (UHV) conditions. Deposition on MgO(001) single-crystal substrates ensured high-quality epitaxial growth, with a base pressure maintained at ~10^{-8} mbar.

For structural, and chemical characterization, $Co_{47}Mn_{32}Si_{21}$/MgO/$Co_{47}Mn_{32}Si_{21}$ multilayers were prepared with a 3 nm MgO insulating barrier between two 20 nm $Co_{47}Mn_{32}Si_{21}$layers. The MgO thickness was optimized to assess interfacial properties and thermal stability, while the $Co_{47}Mn_{32}Si_{21}$ thickness minimized measurement challenges in atom probe tomography (APT). A schematic representation of the designed layer stack is shown in Fig. 1, providing a clear overview of the MTJ architecture investigated in this study. No intermediate annealing steps were performed during deposition. Post-annealing was conducted only after the complete stack growth to ensure uniform thermal treatment of the entire structure. This precisely engineered multilayer system enables a detailed investigation of atomic diffusion, structural evolution, and magnetic behavior while minimizing atom loss during evaporation, providing a comprehensive framework for understanding interfacial interactions and their influence on material performance.

Magnetic tunnel junctions (MTJs) were fabricated following Ishikawa et al. [11], with modifications incorporating CoFe and Tantalum (Ta) for enhanced stability. The MTJs were deposited on MgO (001) single-crystal substrates to promote high-quality epitaxial growth. The layer stack consisted of a 10 nm MgO buffer layer, a 10 nm $Co_{50}Fe_{50}$ buffer (selected for its excellent lattice matching with MgO to ensure epitaxial quality), and a 1 nm Ta interlayer to ensure structural integrity and limit diffusion. The lower ferromagnetic electrode consisted of 5 nm $Co_{47}Mn_{32}Si_{21}$, selected for its high spin polarization. A 3 nm MgO barrier facilitated spin-dependent tunneling, while a symmetric 5 nm $Co_{47}Mn_{32}Si_{21}$ upper electrode optimized TMR. A 1 nm Ta spacer tuned exchange interactions between the free and pinned layers. The pinned layer included a 3 nm $Co_{90}Fe_{10}$ layer, selected for its high saturation magnetization. It forms a strong exchange coupling with the adjacent 10 nm $Ir_{20}Mn_{80}$ antiferromagnetic layer, which ensures stable exchange bias. A 3 nm Ta capping layer was applied to prevent oxidation and enhance durability. Further details on the design rationale and functional role of each layer in the complete MTJ stack are provided in the Supplementary material, Section S1. Structural and atomic-level analyses were carried out using high-resolution transmission electron microscopy (HRTEM), energy-dispersive X-ray spectroscopy (EDS), and atom probe tomography. Tunnel magnetoresistance properties were characterized through direct current four-probe measurements to ensure accurate evaluation of electrical transport behavior.

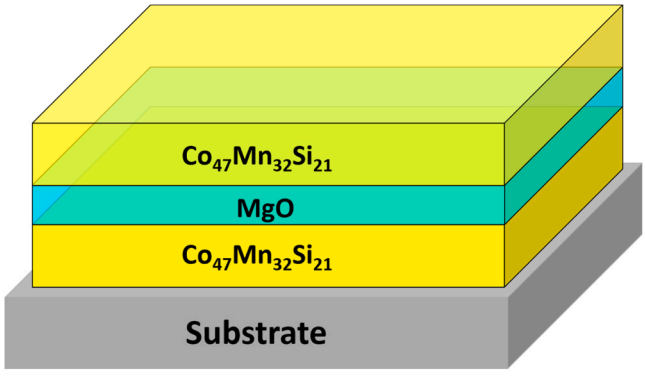

Fig. 1. Schematic illustration of the $Co_{47}Mn_{32}Si_{21}$/MgO/$Co_{47}Mn_{32}Si_{21}$ magnetic tunnel junction architecture deposited on MgO(001) substrate. The structure consists of a 3 nm MgO insulating layer sandwiched between two 20 nm $Co_{47}Mn_{32}Si_{21}$ layers, representing the trilayer configuration used for structural and magnetic analyses.

3. Results and discussion

3.1. Structural and compositional characterization

Fig. 2 presents a series of structural and compositional analyses performed on the as-prepared $Co_{47}Mn_{32}Si_{21}$/MgO/$Co_{47}Mn_{32}Si_{21}$ multilayer structure. For clarity and consistency, $Co_{47}Mn_{32}Si_{21}$ hereafter referred to as CMS. Fig. 2a presents a HRTEM image, offering detailed insights into the structural and compositional characteristics of the multilayer. Contrast variations arise from mass-thickness differences and diffraction effects, with the CMS layers exhibiting stronger contrast than the MgO spacer. The alternating contrast pattern indicates sharp, well-defined interfaces, characteristic of high-quality epitaxial growth with minimal structural imperfections. The MgO layer, having a lower atomic number, appears with reduced contrast, while localized diffraction variations may be attributed to strain or minor defects. Fig. 2b presents EDS elemental mappings, further validating the compositional distribution within the multilayer system. The blue regions correspond to Mg and O, clearly delineating the MgO layers, while the yellow regions highlight the presence of Co, Mn, and Si, confirming the composition of the CMS layers. The distinct elemental separation supports the presence of well-defined heterointerfaces. Thickness measurements reveal that the MgO layers are approximately 3 nm thick, demonstrating precise layer deposition and structural integrity.

APT was performed to further investigate the atomic-scale distribution within the multilayer system. The APT reconstruction in Fig. 2(c) reveals a periodic nanolamellar structure with alternating CMS and MgO layers. In this visualization, CMS rich regions are shown in yellow, while MgO rich regions are depicted in blue, highlighting the compositional contrast. The measured MgO layer thickness is consistent with structural observations from HRTEM and EDS. The sharp, well-defined interfaces confirm the high structural integrity of the multilayer system, with no detectable intermixing at the boundaries.

To quantify the elemental composition within the layers, local cylindrical regions of analysis perpendicular to the oxide layer were extracted, as shown in Fig. 2(c), with the corresponding composition profile presented in Fig. 2(d). On average, the elemental concentrations within the CMS layers were Co: 47 at%, Mn: 32 at%, and Si: 21 at%, while the MgO layers exhibited a composition of Mg: ~50 at% and O: ~50 at%, aligning well with the intended stoichiometry. The homogeneous distribution of elements across the layers further supports the structural uniformity of the multilayer system. No evidence of elemental clustering or compositional anomalies was observed, indicating a well-controlled deposition process. Collectively, these results confirm the successful fabrication of a highly ordered multilayer system with precise structural and compositional integrity.

3.2. Kinetics of Mn grain boundary diffusion in MgO

To further analyze elemental diffusion mechanisms, three-layer samples underwent controlled heat treatments in an ultra-high vacuum furnace, maintaining a residual gas pressure below 1×10^{-7} mbar to facilitate Mn diffusion through the MgO layer. The annealing sequence included five conditions ranging from 673 K to 873 K, with durations decreasing from 48 h to 15 min as the temperature increased. These conditions are summarized in Table 1 for clarity.

Fig. 3a presents an atomic-scale map of the MgO layer after 48 H of

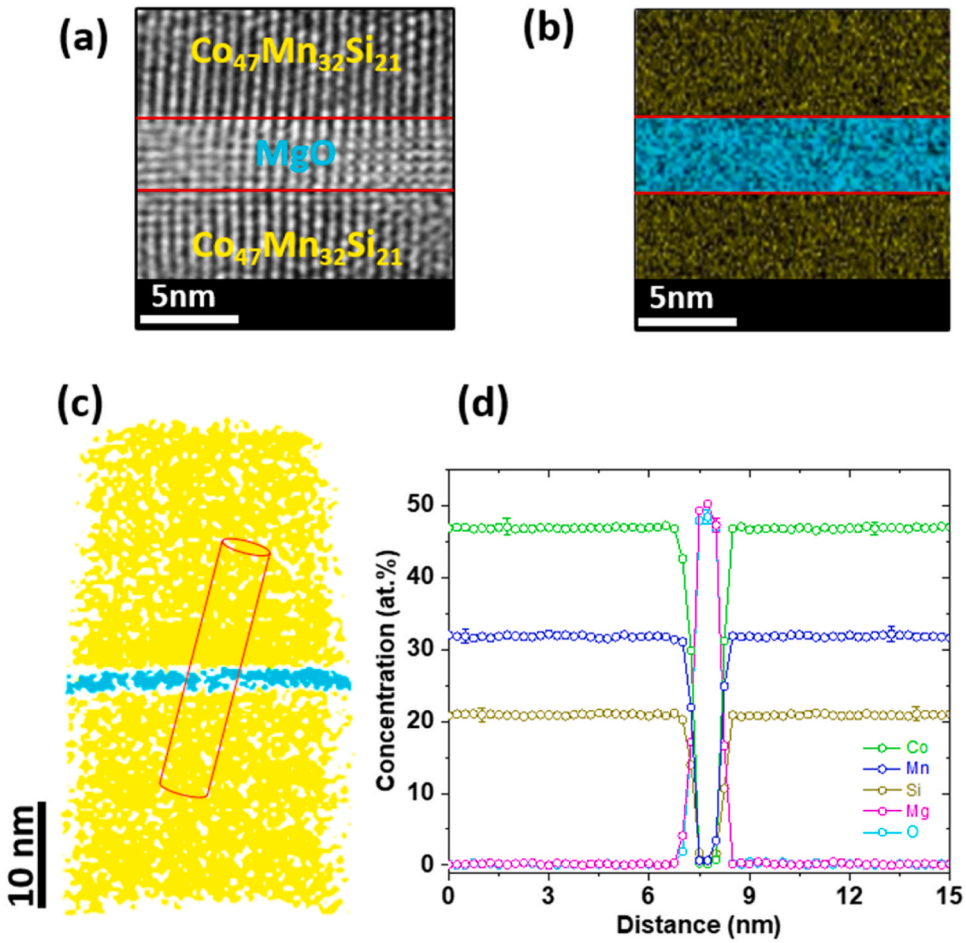

Fig. 2. Characterization of the as-prepared CMS/MgO/CMS heterostructure. **(a)** Cross-sectional HRTEM image showing a well-defined layered structure. **(b)** EDS elemental mapping of Co, Mn, Si, Mg, and O, with CMS highlighted in yellow and MgO in blue. **(c)** APT atomic reconstruction, illustrating the element distribution, consistent with EDS data. The cylinder (diameter: 6 nm) drawn in (**c**) indicates the section used for analysis. **(d)** APT composition profile confirming a sharp CMS/MgO interface, clearly distinguishing variations between the interfaces. In the representative profile shown in (d), the MgO thickness is approximately 2.6 nm, while analysis over multiple regions yields values close to the nominal 3. Error bars mark the 1σ range.

Table 1
Thermal annealing conditions.

Temperature	673 K	723 K	773 K	823 K	873 K
Duration	48 h	24 h	6 h	1 h	15 min

annealing at 673 K, captured in a top-down view along the needle axis, revealing a distinct Mn-enriched grain boundary morphology with laterally oriented boundaries. The grain boundary morphology observed in the present study, characterized by lateral orientation, structural continuity, and a high occurrence of symmetric tilt configurations, closely corresponds to the predictions from first-principles DFT calculations reported in Ref. [21]. The authors identified Σ5(210)[001] symmetric tilt grain boundaries as energetically favorable and structurally stable. The grain sizes determined in the current experiment (approximately 10–15 nm), along with the geometric features of the boundaries, are in good agreement with the DFT-modeled structures. These models further indicate that such grain boundaries can act as preferential pathways for atomic segregation and are associated with localized reductions in the electronic band gap [19].

The schematic representation in the Fig. 3b provides additional insight into the multilayer structure, illustrating the arrangement and distribution of tilted grain boundaries. The direct visualization of Mn accumulation along these boundaries reinforces these findings, providing clear evidence that Mn diffusion within the MgO layer is confined to these regions, highlighting the critical role of grain boundaries as the primary diffusion pathways. Up to 873 K, Mn bulk diffusion from the CMS layer into the MgO layer remains effectively suppressed, with atomic transport occurring predominantly along grain boundaries. To gain deeper insight into this behavior, a cylindrical probe was positioned through a representative grain boundary (see Fig. 3a), enabling a detailed analysis of Mn distribution and diffusion characteristics. The extracted composition profile, shown in Fig. 3c, follows a Gaussian-like distribution, confirming the preferential diffusion of Mn through these pathways. This trend is consistent across different concentrations, with no detectable Mn volume diffusion within the MgO layer up to 873 K.

Although grain growth is not observed within the examined temperature range, annealing promotes Mn accumulation accompanied by gradual structural refinement. This suggests enhanced crystallinity without morphological coarsening. A systematic analysis across annealing stages reveals a gradual increase in Mn concentration over time, highlighting the temperature-dependent nature of diffusion. While Mn accumulation progressively rises with annealing, no significant change in grain size is observed within the examined temperature range. However, this does not rule out microstructural refinement. As established in Ref. [22], thermally activated atomic-scale rearrangements can enhance crystallinity and reduce defect density, even in the absence of grain coarsening. Fig. 3d presents an atomic reconstruction of the MgO layer annealed at this temperature, clearly illustrating the onset of Mn diffusion into the bulk MgO layer. This transition from grain

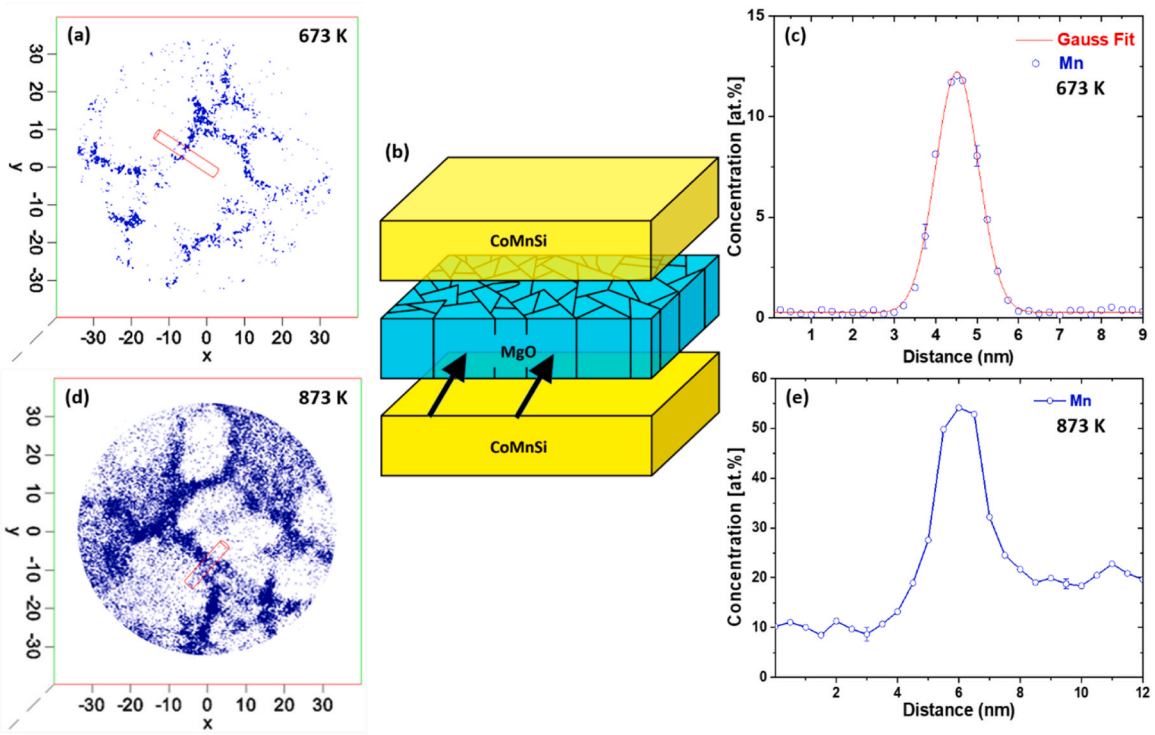

Fig. 3. (a) Atomic-scale reconstruction showing a top-down view of the MgO layer along the needle axis after annealing at 673 K (48 h). **(b)** Schematic illustration of the magnetic tunnel junction structure, showing the CMS/MgO/CMS stack, grain boundaries within the MgO barrier, and the corresponding cross-sectional and plan-view imaging orientations. **(c)** Mn-enriched zone along the MgO grain boundary, fitted using a Gaussian distribution. **(d)** Atomic-scale top-view reconstruction of the MgO layer after annealing at 873 K. **(e)** Concentration depth profile along the MgO grain boundary at 873 K (15 min). The analysis cylinders (6 nm diameter) used for determining composition profiles, marked in **(a)** and **(d)**, reveal grain boundaries distinctly decorated by Mn segregation. Error bars mark the 1σ range.

boundary-limited atomic transport to volume diffusion is further quantified in Fig. 3e, which depicts the corresponding composition profile. The elevated Mn concentration beyond the grain boundaries confirms the initiation of bulk diffusion at 873 K. It should be emphasized that the identification of 873 K as the onset of bulk assisted Mn diffusion is not based on a single one dimensional concentration profile. Rather, it is derived from statistically averaged atom probe tomography concentration profiles obtained from multiple specimens and multiple grain boundary and grain interior regions, with Fig. 3(e) shown as a representative example.

To elucidate the mechanisms contributing to this transition, we considered several thermally activated processes. Although thermal expansion and increased atomic vibrations occur at elevated temperatures, substantial lattice softening of MgO is unlikely at 873 K due to its high melting point (~3125 K) and thermal stability [23,24]. In addition, elevated temperatures can lead to an increase in oxygen vacancy concentrations, which are known to reduce the activation energy for cation migration and thereby promote bulk diffusion [25,26]. Importantly, the cubic rocksalt structure of MgO remains stable beyond 873 K without undergoing any structural phase transition, as confirmed by in situ diffraction studies and thermal expansion measurements [23]. This rules out structural transformation and further supports a defect-driven mechanism for the observed Mn bulk diffusion. Furthermore, saturation of grain boundary diffusion channels may play a key role. At temperatures up to 823 K, Mn diffusion is largely confined to the grain boundaries; however, continued accumulation may approach the solubility limit at 873 K, thereby driving Mn atoms into the bulk lattice [27].

While the onset of bulk diffusion marks a significant transition, grain boundary diffusion remains the dominant atomic transport mechanism at lower temperatures, specifically below 873 K. In this temperature range, the measured diffusion profiles exhibit a temperature-dependent variation and correspond to the C-type diffusion regime, as classified by Harrison [28,29], allowing the determination of individual diffusion coefficients. To further describe this process, the mathematical framework developed by Fisher [30] for concentration dynamics in the source-grain boundary-bulk system can be adapted to the source-grain boundary scenario, expressed as:

$$C(z) = C_0\, Exp\left[\frac{z^2}{4D^{GB}t}\right] \quad (1)$$

here, C_o, $C(z)$, and t represent the initial concentration, the concentration at depth z, and the diffusion time, respectively. The z-coordinate is defined along the grain boundary to determine the short-circuit diffusion coefficient (D^{GB}).

The agreement between the experimentally obtained diffusion profiles and the analytical model in Eq. (1) confirms the time-dependent nature of the diffusion process. Additionally, the logarithmic plot of concentration (C) versus depth squared (z^2) exhibits a clear linear trend (Fig. 4a), further reinforcing its classification within the C-type diffusion regime. As a result, the grain boundary diffusion coefficients of the manganese tracer in the CMS layer were reliably determined, yielding values between 10^{-17} and 10^{-19} cm^2/s, as shown in Fig. 4b. Notably, only data exhibiting strictly grain boundary-controlled Mn transport were considered, while cases where diffusion extended beyond the grain boundaries (Fig. 3(d) were excluded to maintain the focus on grain boundary diffusion behavior. This temperature-dependent diffusion behavior follows an Arrhenius-type relationship, where the diffusion coefficient increases exponentially with temperature, described by:

$$D = D_0\, Exp[\frac{Q}{RT}] \quad (2)$$

where Q is the activation energy, R is the gas constant, and T is the temperature in Kelvin.

The activation energy for Mn grain boundary diffusion in MgO was determined to be 73.11 ± 14 kJ/mol, significantly lower than the values

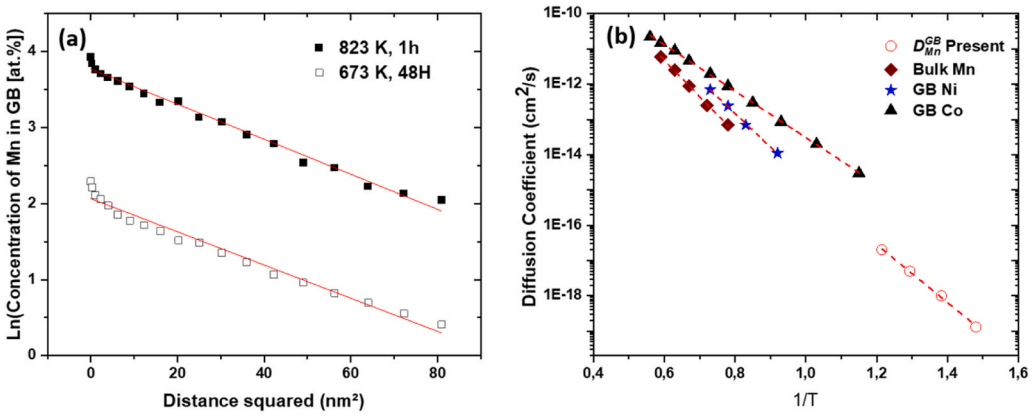

Fig. 4. (a) Typical plots of log C versus z^2 for Mn diffusion along the grain boundary of the MgO layer, annealed at 673 K for 48 h and 823 K for 1 h. The solid lines represent fits according to Eq. (1). **(b)** Temperature dependence of diffusion coefficients in MgO single crystals. The Mn grain boundary diffusion coefficients in MgO are highlighted and compared to the diffusion of various impurity elements in MgO, as reported in previous studies [31,32].

reported for bulk diffusion. Diffusion studies have shown that Mn diffusion in single-crystal MgO requires an activation energy of ~202.6 ± 24.1 kJ/mol [31], while cation diffusion in MgO has been reported in the range of 242–257 kJ/mol [33]. Likewise, Ni grain boundary diffusion in MgO has been associated with an activation energy of 165.94 kJ/mol [32]. These results highlight the substantially lower activation energy associated with Mn grain boundary diffusion, confirming its predominance over bulk lattice diffusion as the primary atomic transport mechanism. This trend aligns with previous research showing that grain boundary diffusion typically requires less activation energy due to the presence of defect-rich interfaces [22]. In MgO, grain boundaries exhibit a high density of vacancies and dislocations, serving as effective diffusion pathways that facilitate Mn migration. The presence of Mn-enriched zones along these boundaries, as observed in Fig. 3a, strongly supports this mechanism, confirming preferential Mn accumulation at these sites. Additionally, cation vacancies within MgO's cubic rocksalt structure further enhance diffusion along defect-rich regions, promoting Mn incorporation [33].

The extent of this effect is strongly influenced by microstructural characteristics, particularly grain size. In this study, the measured grain size ranged from 5 to 15 nm, consistent with the reported 10–15 nm range in polycrystalline MgO films [21]. The higher density of grain boundaries in this size regime offers more efficient atomic transport pathways, thereby enhancing Mn migration along these interfaces and contributing to the lower activation energy observed in this work compared to bulk diffusion. Another key factor governing Mn migration is its strong chemical affinity for oxygen, which promotes the formation of thermodynamically stable Mn-O bonds. This effect becomes more pronounced at elevated temperatures, where diffusion is driven by the chemical potential gradient between CMS and MgO [34]. Previous studies have shown that annealing at 550°C significantly enhances Mn mobility, enabling substantial diffusion over time scales ranging from 20 to 420 min [35]. The presence of oxygen and cation vacancies further facilitates this process by serving as incorporation sites and lowering the activation energy required for Mn migration. Moreover, the close similarity in ionic radii between Mn (~0.83 Å) and Mg (~0.72 Å) makes Mn substitution within the MgO lattice energetically favorable, further promoting diffusion through defect-assisted pathways [36]. These findings highlight the critical role of microstructural features in mass transport mechanisms in oxide materials and provide valuable insights for optimizing diffusion properties in Mn-doped MgO. However, precise control of annealing conditions and Mn concentration is essential, as excessive diffusion may lead to secondary phase formation or alterations in grain boundary chemistry. Additional details on the control of annealing conditions and the resulting grain boundary chemistry are provided in the Supplementary Section 2.

3.3. APT analysis of Mn diffusion in the full MTJ stack

The diffusion analysis discussed above was performed on simplified CMS/MgO/CMS trilayer structures in order to isolate and quantify Mn transport mechanisms at the CMS/MgO interface. To assess whether the diffusion behavior identified in these model systems is also relevant under realistic device conditions, we now extend the analysis to the complete magnetic tunnel junction (MTJ) stack, which incorporates additional functional layers such as CoFe buffers, Ta diffusion barriers, and an IrMn pinning layer.

Fig. 5 summarizes the APT analysis of the complete MTJ stack, comparing the as-prepared state with the annealed condition at 873 K. Fig. 5(a) shows the three-dimensional APT reconstruction of the as-prepared MTJ, revealing a chemically well-defined multilayer architecture with sharp and continuous interfaces. All constituent layers, including CoMnSi, MgO, CoFe, Ta, and IrMn, exhibit a homogeneous elemental distribution, indicating the absence of detectable interdiffusion in the as-deposited state. This observation is further confirmed by the corresponding one-dimensional composition profile shown in Fig. 5 (b). The MgO layer is highlighted by a yellow shaded region, within which no measurable Mn signal is detected. Mn remains fully confined within the CoMnSi electrodes, while the MgO barrier exhibits stoichiometric Mg and O concentrations. The distributions of Ta, Co, Fe, Ir, and Si remain spatially well localized, confirming the chemical stability of the MTJ stack prior to annealing.

In contrast, Fig. 5(c) displays the APT reconstruction of the MTJ after annealing at 873 K, where a pronounced redistribution of Mn is observed. Mn diffusion from the CoMnSi electrodes into the MgO layer becomes clearly evident. An isoconcentration surface corresponding to 62 at% Mn, highlighted in red, is used to visualize the spatial extent of Mn segregation, revealing preferential Mn accumulation within the MgO region. The corresponding composition profile for the annealed MTJ, shown in Fig. 5(d), further confirms this behavior. The MgO layer, again highlighted by a yellow shaded region, exhibits a clear increase in Mn concentration, while the concentrations of Mg and O remain close to stoichiometric values. Importantly, no comparable diffusion of Co, Fe, Ta, Ir, or Si into the MgO layer is observed. This demonstrates that diffusion at 873 K is selective to Mn and occurs specifically within the MgO barrier.

Taken together, these results provide direct experimental evidence that Mn diffusion across the CMS/MgO interface occurs in the under device-relevant annealing conditions and that the diffusion mechanism identified in simplified CMS/MgO/CMS trilayers remains applicable to the complete MTJ stack.

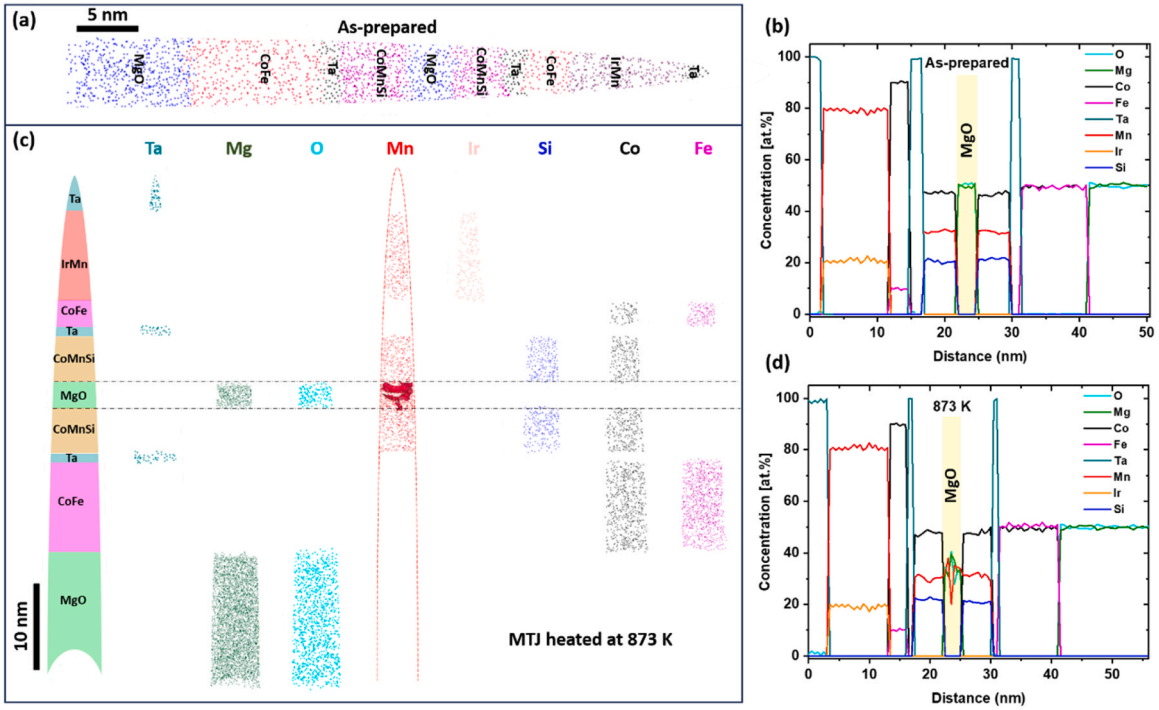

Fig. 5. shows atom probe tomography (APT) results from the complete MTJ stack, comparing the as-prepared state with the annealed condition at 873 K. (a,b) present the APT reconstruction and composition profile of the as-prepared MTJ, revealing a chemically well-defined multilayer structure with no detectable interdiffusion and Mn confined to the CoMnSi electrodes. After annealing at 873 K, (c,d) show pronounced Mn diffusion into the MgO layer. An Mn isoconcentration surface at 62 at% visualizes the spatial extent of Mn segregation, while the corresponding composition profile confirms selective Mn enrichment in MgO, with no detectable diffusion of other elements. All composition profiles were extracted along the analysis direction from the top toward the bottom of the APT tip.

3.4. Crystallinity enhancement and its role in TMR improvement

Building on the insights related to Mn diffusion, we explored how thermally induced structural changes influence spin-polarized transport characteristics in CMS-based magnetic tunnel junctions. To probe this relationship further, $Co_{47}Mn_{32}Si_{21}$-based MTJs were fabricated and characterized using tunneling magnetoresistance measurements, following the device fabrication process described in the experimental section. The TMR curves shown in Fig. 6a, were measured for an as-deposited (non-annealed) device using a bias voltage of 1 mV at 4.2 K and 5 mV at room temperature (RT). A maximum TMR ratios of 1995% at 4.2 K and 378% at room temperature is obtained for the best-performing device under these conditions, significantly surpassing previously reported values of 1135% and 236%, respectively, for Co_2MnSi MTJs grown on MgO (001) single-crystal substrates [11]. To evaluate the reproducibility of the results, six independently fabricated MTJ devices (n = 6) were measured using the same bias voltage, junction dimensions, and magnetic field sweep parameters. At 4.2 K, the measured TMR ratios ranged from 1985% to 1995%, yielding an average value of 1991% with a standard deviation of 4%. At room temperature, the values fell between 360% and 378%, with an average of 366% and a standard deviation of 7%. The relatively small spread in the data confirms good device-to-device consistency. Table 2 compares the present results with representative Co_2MnSi-based MgO MTJs reported in the literature under comparable measurement conditions, explicitly indicating the corresponding temperatures and bias voltages.

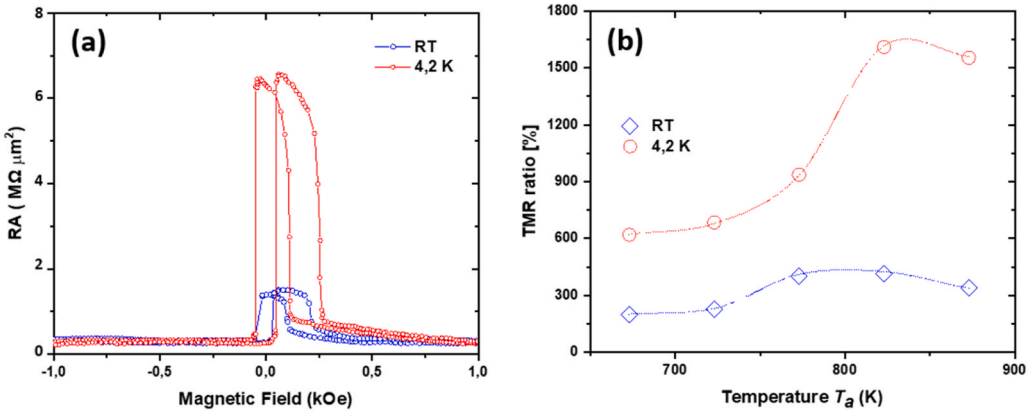

Fig. 6. **(a)** Typical tunnel magnetoresistance curves for a CMS/MgO/CMS MTJ measured at room temperature (blue) with a bias voltage of 5 mV and at 4.2 K (red) with a bias voltage of 1 mV. The device shown is in the as-deposited state, i.e., without post-deposition annealing. The TMR ratios reach 1995% at 4.2 K and 378% at RT. **(b)** TMR ratio as a function of annealing temperature (T_a) for similarly fabricated MTJs, showing a peak at 823 K, beyond which TMR slightly decreases due to interfacial degradation. Measurements were taken at both 4.2 K (1 mV bias) and RT (5 mV bias).

Table 2
Comparison of representative MgO-based MTJs and the present work.

Ref.	MTJ structure	Temperature	TMR (%)	Bias voltage
[10]	Co_2MnSi/MgO/CoFe	2 K	753	1 mV
[10]	Co_2MnSi/MgO/CoFe	RT	217	1 mV
[11]	Co_2MnSi/MgO/Co_2MnSi	4.2 K	1135	1 mV
[11]	Co_2MnSi/MgO/Co_2MnSi	RT	236	5 mV
[38]	Co_2MnSi/MgO/Co_2MnSi	290 K	354	5 mV
[38]	Co_2MnSi/MgO/Co_2MnSi	4.2 K	1135	1 mV
Present work	$Co_{47}Mn_{32}Si_{21}$/MgO/$Co_{47}Mn_{32}Si_{21}$	4.2 K	1985–1995	1 mV
Present work	$Co_{47}Mn_{32}Si_{21}$/MgO/$Co_{47}Mn_{32}Si_{21}$	RT	360–378	5 mV

This significant enhancement results from an optimized buffer layer configuration consisting of MgO substrate, a directly deposited CoFe layer, and a tantalum diffusion barrier positioned atop CoFe. This carefully engineered interface effectively suppresses interdiffusion, maintains a smooth MgO tunnel barrier, and enhances spin-polarized transport, ultimately contributing to the observed giant TMR effect. By minimizing defect-induced scattering at the CoFe/MgO interface, tunneling spin polarization is enhanced, leading to more efficient spin filtering, which is critical for achieving high TMR ratios [5,6]. This effect is particularly significant, as interfacial disorder and oxygen vacancies in the MgO barrier are known to degrade spin-polarized transport [37]. These findings highlight the importance of precise interface engineering in achieving high-performance spintronic devices, with direct implications for next-generation non-volatile memory and magnetic sensing technologies.

The $Co_{47}Mn_{32}Si_{21}$/MgO/$Co_{47}Mn_{32}Si_{21}$ system investigated in the present study achieves record-high TMR values under comparable conditions, underscoring the critical role of material optimization and coherent tunneling. Because thermal processing is a key element of interface engineering, it is important to note that the optimal annealing temperature in MgO-based magnetic tunnel junctions is strongly system dependent. For Co_2MnSi/MgO/Co_2MnSi MTJs, annealing temperatures typically in the range of approximately 723–823 K have been reported to maximize tunnel magnetoresistance through improved chemical ordering and enhanced Δ_1-band coherent tunneling, whereas higher annealing temperatures lead to interfacial intermixing and degradation of transport properties [11,12]. In contrast, CoFeB/MgO-based MTJs generally require lower annealing temperatures of about 600–700 K, since higher temperatures promote boron and tantalum diffusion into the MgO barrier, thereby deteriorating interface quality and TMR performance [15]. In the present $Co_{47}Mn_{32}Si_{21}$/MgO/$Co_{47}Mn_{32}Si_{21}$ system, the peak TMR observed at 823 K together with the onset of Mn bulk diffusion at 873 K therefore defines a system-specific critical annealing temperature that separates beneficial crystallinity enhancement from interface degradation.

Fig. 6b presents the dependence of the tunnel magnetoresistance ratio for CMS-based MTJs, measured at room temperature and 4.2 K as a function of annealing temperature (T_a). The results reveal a substantial enhancement in the TMR ratio with increasing T_a, reaching a maximum at 823 K, followed by a slight decline at 873 K. At 4.2 K, the TMR ratio increases more than twofold between 673 K and 823 K, reaching over 1600% at the optimal annealing temperature of 823 K. A similar trend is observed at room temperature, where the TMR ratio stabilizes around ~410% for T_a between 773 K and 823 K, before slightly decreasing at 873 K. At RT, the TMR ratio remains relatively stable around 410 % between 773 K and 823 K, before slightly decreasing at 873 K. In contrast, at 4.2 K, the TMR ratio shows a marked increase across the same annealing range, rising from approximately 900 % to over 1600 %. This divergence in temperature-dependent response highlights the enhanced spin-polarized tunneling efficiency at low temperatures, which becomes more pronounced with improved atomic ordering and interface quality induced by thermal treatment. The increased low-temperature TMR indicates a reduction in spin scattering and greater coherence in tunneling, both of which are essential for maximizing spin transport in CMS/MgO-based MTJs [8].

The apparent discrepancy between the TMR values in Figs. 6a and 6b stems from the fact that Fig. 6ba represents a single, as-deposited device with pristine interface quality, whereas Fig. 6b illustrates the broader trend based on multiple devices subjected to various annealing temperatures. The device in Fig. 6a benefits from minimal interfacial disorder, enabling maximized spin-polarized tunneling. In contrast, the values in Fig. 6b are averaged across samples and thus reflect the evolution of transport behavior with annealing.

The enhancement of spin polarization observed in the present study arises from a competition between crystallinity improvement and interface stability during thermal annealing. Moderate annealing facilitates atomic-scale rearrangements that improve chemical ordering, reduce interfacial disorder, and promote coherent Δ_1-band tunneling across the CMS/MgO interface. Within this optimal annealing window, Mn diffusion remains largely confined to MgO grain boundaries, thereby preserving the chemical integrity and insulating character of the tunnel barrier. As a result, spin-dependent transport is enhanced and high tunnel magnetoresistance is achieved. At higher annealing temperatures, continued thermal activation leads to excessive Mn segregation and defect accumulation at grain boundaries and interfaces, which alter the local electronic structure by introducing in-gap states and enhanced grain-boundary conductivity. These effects disrupt coherent tunneling and reduce spin polarization, even though crystallinity may continue to improve.

3.5. *Crystallinity and defect suppression*

The progressive improvement in crystallinity and interface quality with increasing T_a facilitates spin-polarized transport by reducing structural disorder, interface trap states, and grain boundary defects [39]. This behavior results from thermally activated atomic mobility during annealing, which enables defect passivation, promotes local atomic ordering, and enhances electronic uniformity at the CMS/MgO interface. Such mechanisms have been widely demonstrated in prior studies [21,22], which show that post-annealing can significantly enhance oxide crystallinity and interfacial quality without requiring grain growth. As a result, the observed peak TMR value at 823 K suggests that annealing within this range optimizes coherent tunneling and spin filtering, thereby maximizing spin polarization at the CMS/MgO interface [40]. The high spin polarization observed in CMS-based MTJs can be attributed to its half-metallic nature, which sets it apart from conventional ferromagnets like CoFe. This distinction is evident in the exceptionally high TMR ratios of up to 1995% at 4.2 K for Co_2MnSi MTJs, compared to 1143% at 10 K for CoFeB/MgO/CoFeB MTJs [41].

While Co_2MnSi achieves high spin polarization due to its intrinsic half-metallicity at E_F, the high TMR ratio in CoFeB/MgO/CoFeB MTJs primarily stems from the coherent tunneling contribution of Δ_1-band electrons [42]. In Co_2MnSi Heusler alloys, compositional variations critically influence both spin polarization and half-metallicity. Theoretical studies suggest that Mn antisites and MnSi antisites are energetically favorable under Mn-rich conditions, with a minimal impact on half-metallicity [43]. In contrast, CoMn antisites introduce unwanted electronic states at the Fermi level and thereby reducing spin polarization. Due to their higher formation energy compared to MnSi antisites, CoMn antisites are effectively suppressed in Mn-rich compositions, helping to preserve high spin polarization and a robust half-metallic nature. Although direct identification of such antisite defects is beyond the resolution of techniques like APT or EDX, the observed correlation between Mn redistribution, improved crystallinity, and

enhanced TMR performance is consistent with prior theoretical predictions regarding the role of antisite disorder in Heusler alloy [43]. However, no direct experimental evidence of antisite defect suppression is provided in the present work, and this effect should be regarded as a possible contributing factor rather than a demonstrated mechanism. Nevertheless, future investigations using site-sensitive techniques, such as neutron diffraction or X-ray absorption spectroscopy, will be essential to directly confirm the presence or suppression of antisite defects.

Despite this thermodynamic tendency, residual CoMn antisites may still form during non-equilibrium growth and annealing, particularly in CMS films deposited at room temperature and annealed between 823 and 873 K, which are unlikely to reach full thermal equilibrium [44]. Under such conditions, Mn redistribution and segregation at interfaces and grain boundaries may influence local chemical disorder, which can locally impair spin-dependent transport. This emphasizes the need for carefully optimized processing conditions to suppress antisite-related disorder and maintain efficient spin transport. In parallel, the observed increase in TMR ratio with annealing up to 823 K suggests that moderate atomic diffusion is associated with improved crystallinity and reduced interface defects, thereby supporting coherent tunneling. The rise in the diffusion coefficient with temperature supports the role of thermally activated atomic ordering in reducing grain boundary disorder and promoting coherent tunneling. However, excessive Mn migration from the Heusler alloy into the MgO barrier could degrade TMR performance by creating conductive pathways at grain boundaries, which compromise the insulating barrier and diminish spin filtering efficiency. While such a drastic concentration shift is unlikely, even limited Mn diffusion into grain boundaries may disrupt the local magnetic order, potentially contributing to reduced tunneling efficiency.

Importantly, at 873 K, we observe the onset of Mn diffusion into the MgO barrier, yet the TMR drop remains modest. This suggests that a critical threshold for barrier disruption has not yet been crossed. Nonetheless, our interpretation is that further annealing beyond 873 K would likely accelerate detectable intermixing within the spatial resolution of APT and grain boundary segregation, thereby promoting more pronounced deterioration of spin polarization and coherent tunneling. At this stage, the decline in TMR correlates with the increased grain boundary diffusion of Mn into the MgO barrier and the onset of interfacial degradation. While moderate annealing improves crystallinity and enhances spin polarization, excessive Mn migration toward grain boundaries can introduce localized defect states, disrupting coherent tunneling. Previous studies on MgO grain boundaries in MTJs have demonstrated that these interfaces act as preferential sites for defect segregation, increasing in-gap states and degrading the insulating properties of MgO [21]. First-principles modeling has further shown that MgO grain boundaries reduce the local tunneling barrier by up to 3 eV, leading to increased grain boundary conductivity and diminished magnetoresistance performance [45]. This suggests that, at higher annealing temperatures, Mn accumulation at MgO grain boundaries contributes to TMR degradation by increasing structural disorder and interfacial chemical modification, which ultimately reducing spin-filtering efficiency. At $T_a > 873$ K, a slight TMR degradation is observed, likely due to the onset of interfacial interdiffusion and structural disorder, which disrupts coherent tunneling [45]. These results underscore the importance of optimizing annealing temperature to achieve high-performance spintronic devices. Excessive thermal treatment can lead to structural degradation and impaired spin transport properties, primarily due to thermally induced chemical modification at the CMS/MgO interface [46,47]. Furthermore, these findings suggest that additional enhancements in TMR performance could be achieved by effectively suppressing tantalum diffusion at elevated annealing temperatures. Therefore, achieving high spin polarization in Co_2MnSi-based MTJs requires precise control of Mn composition and limitation of antisite-related disorder. suppression of CoMn antisite. In addition to composition tuning, annealing temperature plays a pivotal role in optimizing spin-dependent transport properties and TMR by enhancing atomic ordering, reducing structural disorder, and improving interface quality. This highlights the critical need for fabrication conditions that balance crystallinity improvement with interface stability, paving the way for more efficient spintronic devices in next-generation memory and sensing applications. The enhancement of TMR with annealing up to 823 K is primarily governed by conventional annealing effects widely reported in MgO-based MTJ systems, including improved MgO crystallinity and enhanced interface ordering. While Mn redistribution at the CMS/MgO interface provides mechanistic insight into thermally activated interfacial diffusion processes, it should be regarded as a secondary or contributing factor rather than the dominant driving mechanism for TMR enhancement.

4. Conclusion

In summary, this study provides a comprehensive investigation into the structural evolution and spin-dependent transport properties of $Co_{47}Mn_{32}Si_{21}$/MgO/$Co_{47}Mn_{32}Si_{21}$ multilayers, emphasizing how Mn diffusion, annealing, and interface engineering collectively influence spintronic performance. Controlled annealing experiments revealed that Mn diffusion is predominantly grain boundary-driven. Using atom probe tomography, high-angle annular dark-field scanning transmission electron microscopy, and elemental profiling, we performed the first quantitative analysis of Mn grain boundary diffusion from CMS into MgO. The extracted diffusion coefficients and activation energy of 73.11 kJ/mol provide quantitative insight into the thermally activated nature of grain boundary transport, confirming that Mn diffusion occurs preferentially along grain boundary rather than the bulk.

This grain boundary diffusion mechanism significantly influences both structural integrity and spin-dependent transport properties.

Tunneling magnetoresistance measurements revealed exceptionally a maximum TMR ratios of 1995 % at 4.2 K and 378 % at room temperature in as-prepared devices without post-deposition annealing. These values represent some of the highest TMR performances reported for polycrystalline CMS-based magnetic tunnel junctions. The peak TMR observed after annealing at 823 K is attributed to the combined effects of improved crystallinity, optimized interface engineering, and controlled of Mn diffusion confined to grain boundaries, which preserves interface quality, enhances spin polarization, and supports coherent tunneling. In contrast, annealing beyond 873 K is accompanied by Mn migration into the MgO bulk disrupting this balance and contributing to increased structural disorder, and reduction in tunneling efficiency. Dual-condition measurements at both room temperature and 4.2 K, combined with correlative structural and chemical analyses, allowed for a detailed correlation between interfacial chemistry, thermal processing, and spintronic properties. Altogether, these findings underscore the importance of precise thermal control and composition engineering in optimizing spintronic device performance. Achieving the right balance between crystallinity and interface stability is key to enabling efficient spin transport and advancing next-generation spintronic technologies.

CRediT authorship contribution statement

Mohammed Zenati: Visualization, Software, Data curation, Conceptualization. **Djilali Bensaid:** Project administration. **M Reda Chellali:** Writing – review & editing, Writing – original draft, Visualization, Supervision, Project administration, Investigation.

Declaration of Competing Interest

The authors declare that they have no known competing financial interests or personal relationships that could have appeared to influence the work reported in this paper.

Appendix A. Supporting information

Supplementary data associated with this article can be found in the online version at doi:10.1016/j.jallcom.2026.187245.

References

[1] A.D. Kent, D.C. Worledge, A new spin on magnetic memories, Nat. Nanotechnol. 10 (2015) 187–191, https://doi.org/10.1038/nnano.2015.24.

[2] B. Dieny, I.L. Prejbeanu, K. Garello, P. Gambardella, P. Freitas, R. Lehndorff, W. Raberg, U. Ebels, S.O. Demokritov, J. Akerman, A. Deac, P. Pirro, C. Adelmann, A. Anane, A.V. Chumak, A. Hirohata, S. Mangin, S.O. Valenzuela, M.C. Onbaşlı, M. d'Aquino, G. Prenat, G. Finocchio, L. Lopez-Diaz, R. Chantrell, O. Chubykalo-Fesenko, P. Bortolotti, Opportunities and challenges for spintronics in the microelectronics industry, Nat. Electron. 3 (2020) 446–459, https://doi.org/10.1038/s41928-020-0461-5.

[3] S. Li, X. Chen, M. Fattouhi, T. Huang, C. Lv, M.C.H. de Jong, P. Li, D. Zhu, X. Lin, F. Garcia-Sanchez, E. Martinez, S. Mangin, B. Koopmans, W. Zhao, R. Lavrijsen, Interlayer Dzyaloshinskii–Moriya interaction in synthetic ferrimagnets for spiking neural networks, Adv. Sci. (2026), https://doi.org/10.1002/advs.202519110.

[4] J. Mathon, A. Umerski, Theory of tunneling magnetoresistance of an epitaxial Fe/MgO/Fe(001) junction, Phys. Rev. B 63 (2001) 220403, https://doi.org/10.1103/PhysRevB.63.220403.

[5] S.S.P. Parkin, C. Kaiser, A. Panchula, P.M. Rice, B. Hughes, M. Samant, S.-H. Yang, Giant tunnelling magnetoresistance at room temperature with MgO (100) tunnel barriers, Nat. Mater. 3 (2004) 862–867, https://doi.org/10.1038/nmat1256.

[6] S. Yuasa, T. Nagahama, A. Fukushima, Y. Suzuki, K. Ando, Giant room-temperature magnetoresistance in single-crystal Fe/MgO/Fe magnetic tunnel junctions, Nat. Mater. 3 (2004) 868–871, https://doi.org/10.1038/nmat1257.

[7] S. Picozzi, A. Continenza, A.J. Freeman, Co_2MnX (X = Si, Ge, Sn) Heusler compounds: an *ab initio* study of their structural, electronic, and magnetic properties at zero and elevated pressure, Phys. Rev. B 66 (2002) 094421, https://doi.org/10.1103/PhysRevB.66.094421.

[8] Y. Sakuraba, T. Iwase, K. Saito, S. Mitani, K. Takanashi, Enhancement of spin-asymmetry by L21-ordering in Co2MnSi/Cr/Co2MnSi current-perpendicular-to-plane magnetoresistance devices, Appl. Phys. Lett. 94 (2009), https://doi.org/10.1063/1.3068492.

[9] K. Inomata, S. Okamura, R. Goto, N. Tezuka, Large tunneling magnetoresistance at room temperature using a Heusler alloy with the B2 structure, Jpn. J. Appl. Phys. 42 (2003) L419–L422, https://doi.org/10.1143/JJAP.42.L419.

[10] S. Tsunegi, Y. Sakuraba, M. Oogane, K. Takanashi, Y. Ando, Large tunnel magnetoresistance in magnetic tunnel junctions using a Co2MnSi Heusler alloy electrode and a MgO barrier, Appl. Phys. Lett. 93 (2008), https://doi.org/10.1063/1.2987516.

[11] T. Ishikawa, H. Liu, T. Taira, K. Matsuda, T. Uemura, M. Yamamoto, Influence of film composition in Co2MnSi electrodes on tunnel magnetoresistance characteristics of Co2MnSi/MgO/Co2MnSi magnetic tunnel junctions, Appl. Phys. Lett. 95 (2009), https://doi.org/10.1063/1.3272926.

[12] M. Yamamoto, T. Ishikawa, T. Taira, G. Li, K. Matsuda, T. Uemura, Effect of defects in Heusler alloy thin films on spin-dependent tunnelling characteristics of Co_2MnSi/MgO/Co_2MnSi and Co_2MnGe/MgO/Co_2MnGe magnetic tunnel junctions, J. Phys. Condens. Matter 22 (2010) 164212, https://doi.org/10.1088/0953-8984/22/16/164212.

[13] Y. Sakuraba, M. Hattori, M. Oogane, H. Kubota, Y. Ando, A. Sakuma, N.D. Telling, P. Keatley, G. van der Laan, E. Arenholz, R.J. Hicken, T. Miyazaki, Extremely large spin-polarization in Co2MnSi based magnetic tunnel junctions, J. Magn. Soc. Jpn. 31 (2007) 338–343, https://doi.org/10.3379/jmsjmag.31.338.

[14] E.I. Rashba, Theory of electrical spin injection: tunnel contacts as a solution of the conductivity mismatch problem, Phys. Rev. B 62 (2000) R16267–R16270, https://doi.org/10.1103/PhysRevB.62.R16267.

[15] S. Ikeda, J. Hayakawa, Y. Ashizawa, Y.M. Lee, K. Miura, H. Hasegawa, M. Tsunoda, F. Matsukura, H. Ohno, Tunnel magnetoresistance of 604% at 300 K by suppression of Ta diffusion in CoFeB/MgO/CoFeB pseudo-spin-valves annealed at high temperature, Appl. Phys. Lett. 93 (2008), https://doi.org/10.1063/1.2976435.

[16] D.J. Larson, E.A. Marquis, P.M. Rice, T.J. Prosa, B.P. Geiser, S.-H. Yang, S.S. P. Parkin, Manganese diffusion in annealed magnetic tunnel junctions with MgO tunnel barriers, Scr. Mater. 64 (2011) 673–676, https://doi.org/10.1016/j.scriptamat.2010.12.021.

[17] R.C. Sousa, J.J. Sun, V. Soares, P.P. Freitas, A. Kling, M.F. da Silva, J.C. Soares, Temperature dependence and annealing effects on spin dependent tunnel junctions, J. Appl. Phys. 85 (1999) 5258–5260, https://doi.org/10.1063/1.369959.

[18] J. Schmalhorst, H. Brückl, G. Reiss, M. Vieth, G. Gieres, J. Wecker, Temperature stability of Co/Al2O3/Co junctions, J. Appl. Phys. 87 (2000) 5191–5193, https://doi.org/10.1063/1.373291.

[19] M.R. Chellali, S.H. Nandam, H. Hahn, Deformation-induced chemical inhomogeneity and short-circuit diffusion in shear bands of a bulk metallic glass, Phys. Rev. Lett. 125 (2020) 205501, https://doi.org/10.1103/PhysRevLett.125.205501.

[20] X. Mu, M.R. Chellali, E. Boltynjuk, D. Gunderov, R.Z. Valiev, H. Hahn, C. Kübel, Y. Ivanisenko, L. Velasco, Unveiling the local atomic arrangements in the shear band regions of metallic glass, Adv. Mater. 33 (2021), https://doi.org/10.1002/adma.202007267.

[21] J.J. Bean, M. Saito, S. Fukami, H. Sato, S. Ikeda, H. Ohno, Y. Ikuhara, K. P. McKenna, Atomic structure and electronic properties of MgO grain boundaries in tunnelling magnetoresistive devices, Sci. Rep. 7 (2017) 45594, https://doi.org/10.1038/srep45594.

[22] R.W. Balluffi, S.M. Allen, W.C. Carter, Kinetics of Materials, Wiley, 2005, https://doi.org/10.1002/0471749311.

[23] T.F.J. Bögels, R. Caracas, Critical point and supercritical regime of MgO, Phys. Rev. B 105 (2022) 064105, https://doi.org/10.1103/PhysRevB.105.064105.

[24] A.S. Arkhipin, A. Pisch, I.A. Uspenskaya, N. Jakse, A molecular dynamics simulation study of crystalline and liquid MgO, Ceramics 7 (2024) 1187–1203, https://doi.org/10.3390/ceramics7030078.

[25] J. Carrasco, N. Lopez, F. Illas, First principles analysis of the stability and diffusion of oxygen vacancies in metal oxides, Phys. Rev. Lett. 93 (2004) 225502, https://doi.org/10.1103/PhysRevLett.93.225502.

[26] J.U. Reveles, A.M. Köster, S.N. Khanna, C. Quintanar, Surface oxygen diffusion into neutral, cationic, and dicationic oxygen vacancies on MgO(100) surfaces, J. Phys. Chem. C 114 (2010) 12265–12270, https://doi.org/10.1021/jp1040184.

[27] A. Bonkowski, J.A. Kilner, R.A. De Souza, Oxygen grain-boundary diffusion in (La, Sr)$FeO_{3-\delta}$ perovskite-oxides probed by molecular-dynamics simulations, RSC Appl. Interfaces 1 (2024) 699–710, https://doi.org/10.1039/D3LF00263B.

[28] L.G. Harrison, Influence of dislocations on diffusion kinetics in solids with particular reference to the alkali halides, Trans. Faraday Soc. 57 (1961) 1191, https://doi.org/10.1039/tf9615701191.

[29] M.R. Chellali, Z. Balogh, H. Bouchikhaoui, R. Schlesiger, P. Stender, L. Zheng, G. Schmitz, Triple junction transport and the impact of grain boundary width in nanocrystalline Cu, Nano Lett. 12 (2012) 3448–3454, https://doi.org/10.1021/nl300751q.

[30] J.C. Fisher, Calculation of diffusion penetration curves for surface and grain boundary diffusion, J. Appl. Phys. 22 (1951) 74–77, https://doi.org/10.1063/1.1699825.

[31] R.A. Weeks, A. Chatelain, Electron paramagnetic resonance spectroscopy applied to diffusion of Mn^{2+} in MgO, J. Am. Ceram. Soc. 61 (1978) 297–301, https://doi.org/10.1111/j.1151-2916.1978.tb09313.x.

[32] R.M. Bunch, W.P. Unruh, M.V. Iverson, Light scattering measurements of diffusional growth of precipitates in nickel- and cobalt-doped MgO, J. Appl. Phys. 58 (1985) 1474–1482, https://doi.org/10.1063/1.336079.

[33] J.A. Van Orman, K.L. Crispin, Diffusion in oxides, Rev. Mineral. Geochem. 72 (2010) 757–825, https://doi.org/10.2138/rmg.2010.72.17.

[34] D.A. de Abreu, O. Fabrichnaya, Thermodynamic modeling of the Mn–Si–O system, Phys. Chem. Min. 52 (2025) 2, https://doi.org/10.1007/s00269-024-01302-8.

[35] M.A.I. Nahid, M. Oogane, H. Naganuma, Y. Ando, Structural and magnetic properties of Co_2MnSi Heusler alloy thin films on Si, Jpn. J. Appl. Phys. 48 (2009) 083002, https://doi.org/10.1143/JJAP.48.083002.

[36] R.D. Shannon, Revised effective ionic radii and systematic studies of interatomic distances in halides and chalcogenides, Acta Crystallogr. Sect. A 32 (1976) 751–767, https://doi.org/10.1107/S0567739476001551.

[37] M.G. Münzenberg, Ferromagnets stirred up, Nat. Mater. 9 (2010) 184–185, https://doi.org/10.1038/nmat2706.

[38] H. Liu, Y. Honda, T. Taira, K. Matsuda, M. Arita, T. Uemura, M. Yamamoto, Giant tunneling magnetoresistance in epitaxial Co2MnSi/MgO/Co2MnSi magnetic tunnel junctions by half-metallicity of Co2MnSi and coherent tunneling, Appl. Phys. Lett. 101 (2012), https://doi.org/10.1063/1.4755773.

[39] M. Salaheldeen, M. Ipatov, P. Corte-Leon, V. Zhukova, A. Zhukov, Effect of annealing on the magnetic properties of Co2MnSi-based heusler alloy glass-coated microwires, Metals 13 (2023) 412, https://doi.org/10.3390/met13020412.

[40] Y. Sakuraba, K. Izumi, T. Iwase, S. Bosu, K. Saito, K. Takanashi, Y. Miura, K. Futatsukawa, K. Abe, M. Shirai, Mechanism of large magnetoresistance in Co_2MnSi/Ag/Co_2MnSi devices with current perpendicular to the plane, Phys. Rev. B 82 (2010) 094444, https://doi.org/10.1103/PhysRevB.82.094444.

[41] T. Scheike, Z. Wen, H. Sukegawa, S. Mitani, 631% room temperature tunnel magnetoresistance with large oscillation effect in CoFe/MgO/CoFe(001) junctions, Appl. Phys. Lett. 122 (2023), https://doi.org/10.1063/5.0145873.

[42] J.D. Burton, S.S. Jaswal, E.Y. Tsymbal, O.N. Mryasov, O.G. Heinonen, Atomic and electronic structure of the CoFeB/MgO interface from first principles, Appl. Phys. Lett. 89 (2006), https://doi.org/10.1063/1.2360189.

[43] S. Picozzi, A. Continenza, A.J. Freeman, Role of structural defects on the half-metallic character of Co_2MnGe and Co_2MnSi Heusler alloys, Phys. Rev. B 69 (2004) 094423, https://doi.org/10.1103/PhysRevB.69.094423.

[44] B. Hülsen, M. Scheffler, P. Kratzer, Thermodynamics of the Heusler alloy $Co_{2-x}Mn_{1+x}Si$: a combined density functional theory and cluster expansion study, Phys. Rev. B 79 (2009) 094407, https://doi.org/10.1103/PhysRevB.79.094407.

[45] Y. Henry, S. Mangin, T. Hauet, F. Montaigne, Positive exchange-bias induced by interface domain wall quenching in GdFe/TbFe films, Phys. Rev. B 73 (2006) 134420, https://doi.org/10.1103/PhysRevB.73.134420.

[46] G. Landry, Y. Dong, J. Du, X. Xiang, J.Q. Xiao, Interfacial capacitance effects in magnetic tunneling junctions, Appl. Phys. Lett. 78 (2001) 501–503, https://doi.org/10.1063/1.1336816.

[47] K. Masuda, H. Itoh, Y. Miura, Interface-driven giant tunnel magnetoresistance in (111)-oriented junctions, Phys. Rev. B 101 (2020) 144404, https://doi.org/10.1103/PhysRevB.101.144404.